



**HAL**  
open science

# Investigation of magnetite-Co interactions: from environmentally relevant trace Co levels to core-shell Fe<sub>3</sub>O<sub>4</sub>@Co(OH)<sub>2</sub> nanoparticles with magnetic applications

Laura Fablet, Fadi Choueikani, Mathieu Pédrot, Margaux Kerdiles, Mathieu Pasturel, Rémi Marsac

## ► To cite this version:

Laura Fablet, Fadi Choueikani, Mathieu Pédrot, Margaux Kerdiles, Mathieu Pasturel, et al.. Investigation of magnetite-Co interactions: from environmentally relevant trace Co levels to core-shell Fe<sub>3</sub>O<sub>4</sub>@Co(OH)<sub>2</sub> nanoparticles with magnetic applications. *Environmental science.Nano*, 2023, 10 (11), pp.3051-3061. 10.1039/d3en00379e . insu-04206732

**HAL Id: insu-04206732**

**<https://insu.hal.science/insu-04206732>**

Submitted on 14 Sep 2023

**HAL** is a multi-disciplinary open access archive for the deposit and dissemination of scientific research documents, whether they are published or not. The documents may come from teaching and research institutions in France or abroad, or from public or private research centers.

L'archive ouverte pluridisciplinaire **HAL**, est destinée au dépôt et à la diffusion de documents scientifiques de niveau recherche, publiés ou non, émanant des établissements d'enseignement et de recherche français ou étrangers, des laboratoires publics ou privés.



Distributed under a Creative Commons Attribution - NonCommercial 4.0 International License

# Environmental Science Nano

Accepted Manuscript

This article can be cited before page numbers have been issued, to do this please use: L. Fablet, F. Choueikani, M. Pédrot, M. Kerdiles, M. Pasturel and R. Marsac, *Environ. Sci.: Nano*, 2023, DOI: 10.1039/D3EN00379E.



This is an Accepted Manuscript, which has been through the Royal Society of Chemistry peer review process and has been accepted for publication.

Accepted Manuscripts are published online shortly after acceptance, before technical editing, formatting and proof reading. Using this free service, authors can make their results available to the community, in citable form, before we publish the edited article. We will replace this Accepted Manuscript with the edited and formatted Advance Article as soon as it is available.

You can find more information about Accepted Manuscripts in the [Information for Authors](#).

Please note that technical editing may introduce minor changes to the text and/or graphics, which may alter content. The journal's standard [Terms & Conditions](#) and the [Ethical guidelines](#) still apply. In no event shall the Royal Society of Chemistry be held responsible for any errors or omissions in this Accepted Manuscript or any consequences arising from the use of any information it contains.

# Investigation of magnetite-Co interactions: from environmentally relevant trace Co levels to core-shell $\text{Fe}_3\text{O}_4@\text{Co}(\text{OH})_2$ nanoparticles with magnetic applications

Laura Fablet<sup>1,2</sup>, Fadi Choueikani<sup>2</sup>, Mathieu Pédrot<sup>1</sup>, Margaux Kerdiles<sup>1</sup>, Mathieu Pasturel<sup>3</sup> and Rémi Marsac<sup>1\*</sup>

<sup>1</sup> Univ Rennes, CNRS, Géosciences Rennes – UMR 6118, F-35000 Rennes, France

<sup>2</sup> Synchrotron SOLEIL, l'Orme des Merisiers, Départementale 128, 91190 Saint-Aubin, France

<sup>3</sup> Univ Rennes, CNRS, ISCR – UMR 6226, F-35000, Rennes, France

(\*corresponding author: remi.marsac@cnrs.fr)

## Abstract

View Article Online  
DOI: 10.1039/D3EN00379E

Magnetite (Fe<sub>3</sub>O<sub>4</sub>) nanoparticles (MNs) are largely known as strong sorbents for inorganic ions such as divalent transition metals (e.g. Co<sup>2+</sup>). Therefore, MNs play an important role on the behavior and fate of trace contaminants, and are commonly used in contaminated water treatment technologies. In addition, surface modification of MNs using Co<sup>2+</sup> affects MNs magnetic properties, which leads to a broad range of high technology applications (e.g., catalysis, medicine and electronics). However, the mechanisms involved between fully stoichiometric magnetite (i.e., with Fe(II)/Fe(III) = 0.5) and transition metals in aqueous solutions are still poorly understood. Adsorption of Co onto stoichiometric MNs (~10 nm-sized) was studied at pH = 8 under inert atmosphere to ensure no evolution of MNs stoichiometry. The Co adsorption isotherm was found non-linear over the 5 orders of magnitude in aqueous [Co] investigated. Adsorption modeling, soft X-ray absorption spectroscopy (XAS) and magnetic circular dichroism (XMCD) at the Co and Fe L<sub>2,3</sub>-edges evidenced three types of surface species, which could be attributed to (i) surface complexed or incorporated Co<sup>2+</sup> with a ferrimagnetic behavior at low loadings, (ii) magnetically-silent small Co polymers at intermediate loadings and (iii) precipitation of antiferromagnetic Co(OH)<sub>2(s)</sub>-like phase onto the magnetite surface for highest Co concentrations. These results might not only help predicting behavior and fate of Co in the environment, but also to optimize the synthesis procedures of Co-modified MNs using water as solvent for high technology applications.

## Environmental Significance

View Article Online  
DOI: 10.1039/D3EN00379E

In natural environments, magnetite nanoparticles are present in many types of soil. These iron oxide nanoparticles are known to affect the speciation of contaminants and be used for remediation purposes. However, surface reactivity of stoichiometric magnetite towards metal ions like  $\text{Co}^{2+}$ , defined by a  $\text{Fe(II)/Fe(III)} = 0.5$ , has rarely been studied in the absence of oxygen that can oxidize its surface to maghemite. Adsorption isotherms, X-ray absorption spectroscopy and X-ray magnetic circular dichroism evidenced three different Co surface species, which modified the magnetic properties of the nanoparticles. This work sheds light on the interaction mechanisms of magnetite and  $\text{Co}^{2+}$  in aqueous media, which might help predicting the environmental fate of Co, and provide some guidelines for the environmentally-friendly synthesis of core-shell  $\text{Fe}_3\text{O}_4@\text{Co(OH)}_2$  nanoparticles for magnetic applications.

## 1. Introduction

View Article Online  
DOI: 10.1039/D3EN00379E

Magnetite ( $\text{Fe}_3\text{O}_4$ ) is one of the most abundant iron oxides in the environment, occurring in soils and waters, but also in some living organisms such as bacteria and some animals.<sup>1–5</sup> Magnetite nanoparticles also attract particular interest for many applications (environmental, electronic, medical, agricultural, etc.) due to their unique electronic and structural properties.<sup>6–9</sup> Magnetite is a ferrimagnetic mineral form of Fe oxide, with the chemical composition formula  $\text{Fe}^{2+}(\text{Fe}^{3+})_2(\text{O}^{2-})_4$ , and it has an inverse spinel structure with octahedral sites shared by Fe(II) and Fe(III) cations and tetrahedral sites occupied by Fe(III).<sup>8,10,11</sup> The occurrence of the two Fe oxidation states has major consequences on magnetite properties, notably its redox reactivity<sup>12,13</sup> and magnetic properties.<sup>14–16</sup> Combined with the small size, surface-to-volume ratio<sup>6,17,18</sup> and subsequent high sorption capacity for ions and molecules, magnetite nanoparticles have been widely investigated as contaminant scavengers in natural systems, for water treatment purposes,<sup>8</sup> as support for catalysts<sup>19</sup> or as drug carriers,<sup>20</sup> for instance. Both fields of environment and electronics focus on the sorption of metal ions onto magnetite nanoparticles. In particular, Co is a trace metal that can cause many environmental and health problems,<sup>21–23</sup> and its sorption onto magnetite may (i) influence its transport, mobility and toxicity in natural waters and soils or (ii) be used for remediation purposes.<sup>8</sup> Surface-bound Co may improve the magnetic properties of magnetite nanoparticles, by decreasing their magnetic anisotropy at ambient temperature, while keeping a small size,<sup>24–26</sup> which is of great interest for magneto-optic devices,<sup>27,28</sup> electronic devices,<sup>29</sup> data storage,<sup>26,30,31</sup> high-density recording<sup>32</sup> or even for replacing the rare earths contained in certain permanent magnets.<sup>26,33</sup>

According to the metal concentration and the synthesis method, different metal ions sorption mechanisms onto magnetite exist, such as incorporation,<sup>26,34–37</sup> surface complexation<sup>34,38</sup> and surface precipitation.<sup>39,40</sup> Interaction mechanisms between Co and nanomagnetite surface must be elucidated in environmentally relevant conditions (e.g., in water, at low temperature), which might help deciphering the environmental fate of Co but also inspire environmentally friendly synthesis of Co bound to magnetite particles. However, data are missing due to the experimental challenges associated with the study of magnetite, and their high sensitivity to oxidation and incongruent dissolution of Fe(II) in circumneutral pH conditions.<sup>41,42</sup> By contrast with studies focused on redox reactivity of magnetite,<sup>12,13,43</sup> little effort has been made to preserve the full stoichiometry of magnetite nanoparticles (i.e. Fe(II)/Fe(III) = 0.5) in Co-magnetite adsorption studies.<sup>44–47</sup> However, partial oxidation or Fe(II)-depletion at the surface might drastically impact the adsorption extent and surface Co binding mechanisms, as recently evidenced for redox-inert organic molecules.<sup>48,49</sup>

The present study investigates the sorption of Co onto stoichiometric magnetite nanoparticles in aqueous suspensions, with the aims to (i) elucidate the mechanisms involved at various Co concentrations (e.g., surface complexation, oligomerization, precipitation) and (ii) relate the Co surface speciation to its effects on the electronic and magnetic properties of the nanoparticles. To do so, sorption isotherm experiments have been conducted at pH 8 under an inert atmosphere and modeling has been performed to support results. This pH value was chosen in order to preserve the magnetite stoichiometry, because H<sup>+</sup>-promoted dissolution of Fe<sup>2+</sup> can occur at lower pH values.<sup>41,42</sup> The samples have been characterized by X-ray absorption spectroscopy (XAS) and magnetic circular dichroism (XMCD) at Fe and Co L<sub>2,3</sub>-edges. The results provide important data for the prediction of Co fate in environmental systems where magnetite occurs, as well as key understanding for the development of innovative procedures for the environmentally friendly synthesis of magnetite-bound Co.

## 2. Materials and Methods

### 2.1. Chemicals

All chemicals used were purchased from Sigma-Aldrich and were of analytical grade or better. Sample solutions were prepared with "MilliQ" ultrapure water (specific resistivity 18.2 MΩ cm). All experiments were performed in an anaerobic chamber (N<sub>2</sub>-glovebox, JACOMEX, O<sub>2(g)</sub> < 1 ppm) and all solutions were purged with N<sub>2(g)</sub> for at least 12 hours inside the glovebox before use. All samples were also adjusted pH by HCl and NaOH (no buffer was used). For MET measurements, hexadecyltrimethylammonium bromide (CTAB) was used as surfactant.

### 2.2. Synthesis of stoichiometric magnetite nanoparticles

Stoichiometric magnetite (Fe<sub>3</sub>O<sub>4</sub>) was synthesized, at room temperature, in an N<sub>2</sub>-glovebox (N<sub>2</sub>-glovebox, JACOMEX, O<sub>2(g)</sub> < 1 ppm) by co-precipitation of iron salts.<sup>50</sup> The synthesis method is similar to that used by Demangeat *et al.* (2018)<sup>51</sup> and Jungcharoen *et al.* (2021).<sup>41</sup> First, FeCl<sub>2</sub> and FeCl<sub>3</sub> were dissolved in HCl. Then, the two solutions were mixed to obtain an iron solution with a molar ratio Fe(II)/Fe(III) = 0.5. This solution was added into a NaOH solution leading to the instantaneous precipitation of ~10 nm magnetite nanoparticles. After synthesis, the solid phase was washed using water at pH = 8 and the stoichiometry of magnetite was checked by spectrophotometric determination of dissolved [Fe(II)] and total [Fe] (i.e. [Fe(III)] + [Fe(II)]) by the 1-10 phenanthroline colorimetric method.<sup>52,53</sup>

### 2.3. Sorption experiments

All the samples were prepared in anaerobic conditions, under the same conditions as the magnetite synthesis. A 100 mM CoCl<sub>2</sub> stock solution was prepared. Samples consisted of magnetite aqueous suspensions, for a total Fe concentration of 6.5 mM (~0.5 g L<sup>-1</sup> of

1  
2  
3  
4  
5  
6  
7  
8  
9  
10  
11  
12  
13  
14  
15  
16  
17  
18  
19  
20  
21  
22  
23  
24  
25  
26  
27  
28  
29  
30  
31  
32  
33  
34  
35  
36  
37  
38  
39  
40  
41  
42  
43  
44  
45  
46  
47  
48  
49  
50  
51  
52  
53  
54  
55  
56  
57  
58  
59  
60

Open Access Article Published on 13 September 2023. Downloaded on 3/12/24 AM. This article is licensed under a Creative Commons Attribution-NonCommercial 3.0 Unported Licence.



magnetite), in 15 mL polypropylene tubes, and total Co concentrations ( $[Co]_{tot}$ ) ranging from 0.01 to 3 mM, in 10 mM NaCl solutions. The pH of all samples has been adjusted to 8 by addition of small volumes of 0.1 M HCl or NaOH solutions. Once the pH is stabilized after 7 days, a magnet was used to collect the solid fraction of the samples. The supernatant was filtered at 0.2  $\mu$ m cellulose acetate filters (Sartorius Minisart).

Cobalt concentrations were determined using a UV-Vis spectrophotometric method, adapted from Zahir and Keshtkar (1998).<sup>54–56</sup> It is based on the complexation of  $Co^{2+}$  by 1-Nitroso-2-naphthol-3,6-disulfonic acid disodium salt hydrate (nitroso-R salt). A 1% solution was prepared by dissolving 1g of the nitroso-R salt powder in 100 mL ultrapure water. A volume of 500  $\mu$ L of the nitroso-R solution is added to the sample, with 1mL of a 1 mol L<sup>-1</sup> acetate/acetic acid pH-buffer solution (pH = 4.1), as well as ultrapure water to reach a total volume of 10 mL. The absorbance was recorded at 520 nm with a Shimadzu UV2600 spectrophotometer. A cobalt calibration curve was determined, with concentrations ranging from 5 to 100  $\mu$ M, for the quantification of aqueous Co concentration in the filtered solutions ( $[Co]_{aq}$ ). For the samples with  $[Co]_{aq}$ , a quadrupole ICP-MS (Agilent Technologies 7700X) was used. Before Co quantification, calibration curves were performed and validated using certified material references (SLRS-6, National Research Council). A rhodium solution was used as an internal standard to correct the instrumental drift and potential matrix effects. The limit of Co quantification was determined at 18  $\mu$ M (1.04 ppt) (AFNOR Certification).<sup>57</sup>

The total amount of Co associated with the solid phase was expressed in term of Co surface density onto magnetite ( $[Co]_s$ , in atom nm<sup>-2</sup>) and calculated as follows:

$$[Co]_s = ([Co]_{tot} - [Co]_{aq}) * \frac{V}{m} * \frac{1}{SSA} * N_A * 10^{-18} \quad (1)$$

where  $[Co]_{tot}$  and  $[Co]_{aq}$  are given in mol L<sup>-1</sup>, V is the sample volume (L), m is the magnetite mass (g), SSA is the surface specific area (m<sup>2</sup> g<sup>-1</sup>) and  $N_A$  is the Avogadro constant (mol<sup>-1</sup>).

A Co-hydroxide suspension was prepared from the 100 mM  $CoCl_2$  stock solution which was neutralized by adding NaOH until precipitation, in a N<sub>2</sub>-glovebox, at room temperature. NaOH was added until pH was stable at 10 and the solution was kept as is.

#### 2.4. Characterization by TEM and XRD

Magnetite nanoparticles were characterized by transmission electron microscopy (TEM; Jeol JEM 2100 HR microscope), for three Co concentrations ( $[Co]_{tot} = 0.04, 0.8$  and 3 mM). A small volume of Co-magnetite was collected and a surfactant (CTAB, 1 mM) was added in each sample to limit particle aggregation, which was then diluted with ultrapure water (at pH = 8).





Each sample was sonicated for 15 min. A droplet of the diluted suspension was deposited on a Holey carbon film 300 mesh copper grid and dried inside the anaerobic chamber. Samples were transported to the microscope in hermetically sealed glass bottles, preserving them under an N<sub>2</sub> atmosphere. The average particle diameter of the pristine magnetite was found equal to 11.5±1.5, by measuring 100 particles.<sup>41,42</sup>

Powder X-ray diffraction (XRD) was performed on a Bruker D8 Advance diffractometer working with monochromatized Cu K $\alpha$ 1 radiation ( $\lambda = 0.15406$  nm). The energy detection of the LynxEye detector was settled in order to avoid the fluorescence background from Fe- and Co-atoms. The Co-magnetite solid phases were separated from the solution using a magnet and then deposited and dried on a disoriented Si single crystal holder in an anaerobic chamber. The dried samples were covered by a drop of glycerol to limit the oxidation of magnetite during the XRD analysis.

## 2.5. XAS and XMCD analyses

The solid samples were analyzed by XAS and XMCD, that are covering the soft X-ray range and probing the L<sub>2,3</sub> (2p  $\rightarrow$  3d) absorption edges of Fe and Co transition metals. Thanks to their chemical selectivity and valence state sensitivity, XAS and XMCD give direct information on the electronic and magnetic properties, allowing to better understand the contribution of both Co and Fe cations in the structure and the magnetic behavior of the nanoparticles.

XAS and XMCD spectra at Fe and Co L<sub>2,3</sub> edges were recorded on the DEIMOS beamline at synchrotron SOLEIL.<sup>58</sup> All measurements were performed on dried nanoparticles. To do this, colloidal suspensions were drop-casted on silicon plates and dried at room temperature, in an Ar-glove box (JACOMEX, O<sub>2</sub>(g) < 1ppm) connected to the DEIMOS end-station. The silicon plates are then fixed on a copper sample holder. This one is introduced into the superconducting magnet as end-station. All spectra were collected in Total Electron Yield (TEY) at 4 K and in UHV conditions (10<sup>-10</sup> mbar). The XAS spectra were recorded following the measurements protocol detailed in previous works.<sup>26,41,59</sup> XAS were collected by flipping both the circular polarization of X-rays right ( $\sigma_R$ ) or left ( $\sigma_L$ ), and the external magnetic field (H = +6 or -6 Tesla). Isotropic XAS spectra were plotted as  $(\sigma^+ + \sigma^-)/2$ , while XMCD were plotted as  $(\sigma^+ - \sigma^-)$ , where  $\sigma^+ = [\sigma_L(H^+) + \sigma_R(H^-)]/2$  and  $\sigma^- = [\sigma_L(H^-) + \sigma_R(H^+)]/2$ . XAS and XMCD were normalized by dividing the raw signal by the edge jump of the isotropic XAS. For the all the Co concentrations, the background of XAS and XMCD at Co L<sub>2,3</sub> edges were corrected by subtracting from the raw signal the XAS and XMCD of the pure magnetite (without cobalt) sample measured at Co edges.

1  
2  
3  
4  
5  
6  
7  
8  
9  
10  
11  
12  
13  
14  
15  
16  
17  
18  
19  
20  
21  
22  
23  
24  
25  
26  
27  
28  
29  
30  
31  
32  
33  
34  
35  
36  
37  
38  
39  
40  
41  
42  
43  
44  
45  
46  
47  
48  
49  
50  
51  
52  
53  
54  
55  
56  
57  
58  
59  
60

XMCD magnetization curves at specific sites of Co and Fe  $L_3$  edges were plotted by collecting XMCD intensity as a function of the external magnetic field (from +6 to -6 T). At DEIMOS beamline, the fully circularly polarized X-rays are provided by Apple-II HU52 undulator for XAS and XMCD while EMPHU65 with a polarization flipping rate of 10 Hz was used to record the magnetization curves. The beam size was  $800 \times 800 \mu\text{m}^2$  and the photon energy resolution was 100 meV.

## 2.6. Chemical speciation modeling

Aqueous chemical speciation calculations were performed using the geochemical code PHREEQC (version 2<sup>60</sup>) and the Minteq.v4 database, which accounts for the relevant complexation reaction for  $\text{Co}^{2+}$  with  $\text{Cl}^-$  on  $\text{OH}^-$ , and can predict the solubility of Co-bearing phases (e.g.  $\text{Co}(\text{OH})_{2(\text{s})}$ , whose logarithm of solubility product equals 13.094). Ionic strength effects on equilibrium constants were calculated using the Davies equation.

## 3. Results and Discussion

### 3.1. Cobalt adsorption onto magnetite

The sorption isotherm of Co onto magnetite evidences two distinct behaviors at low and high  $[\text{Co}]_{\text{tot}}$ , when plotted using linear scales (Fig. 1a; data in Table S1). At low  $[\text{Co}]_{\text{tot}}$ , Co interacts strongly with magnetite surface, as shown by the increase in  $[\text{Co}]_{\text{s}}$ , and the corresponding small  $[\text{Co}]_{\text{aq}}$  remaining in the aqueous phase. The sorption of Co reaches a plateau at around  $[\text{Co}]_{\text{s}}$  7 to 10 atom  $\text{nm}^{-2}$ . This value is larger than that of previous studies dedicated to Co adsorption to magnetite under oxidizing conditions at pH 8, in which a sorption plateau was measured at  $1.5 \leq [\text{Co}] \leq 3.3$  atom  $\text{nm}^{-2}$ ,<sup>44–46</sup> and suggests a higher sorption capacity of magnetite as compared to its oxidation product, maghemite. This value compares well with an occupancy of 50% of cation-reactive magnetite surface sites (i.e. 14.84 sites  $\text{nm}^{-2}$ , according to Morelova and al.<sup>61</sup>), if assuming a 1:1 Co:surface site stoichiometry. However, the prevalence of a 1:1 surface complex is very unlikely: multidentate binding might be more favorable because stronger complexes generally form at Fe oxide surfaces.<sup>61–63</sup> In addition, high cation surface loadings generate strong positive surface charge. Therefore, to achieve a cation surface loading of 7 atom  $\text{nm}^{-2}$ , not only magnetite-bound Co-monomers but also small oligomers might form.<sup>64–66</sup>

The plateau in the isotherm is followed by a non-linear increase of  $[\text{Co}]_{\text{s}}$  for  $[\text{Co}]_{\text{aq}}$  above  $\sim 0.2$  mM (Fig. 1a). This corresponds to 10% of Co solubility limit (i.e. 2.4 mM) in 10 mM NaCl solution at pH 8, as calculated with PHREEQC. The non-ideal adsorption behavior, the  $[\text{Co}]_{\text{aq}}$  value and the surface site occupancy point to a surface precipitation mechanism.<sup>67–71</sup> This was confirmed by TEM imaging, showing crystallized sphere-like magnetite nanoparticles of about



10 nm surrounded by an amorphous layer whose thickness was about 1 to 1.5 nm for  $[\text{Co}]_s = 8.30$  and  $25.74$  atom  $\text{nm}^{-2}$ . Such a layer was hardly observed at lower loading (e.g.  $[\text{Co}]_s = 0.12$  atom  $\text{nm}^{-2}$ ; Fig. S1). XRD patterns of the pristine magnetite and with high Co loading ( $25.74$  atom  $\text{nm}^{-2}$ ) were similar, which further support the formation of amorphous  $\text{Co}(\text{OH})_{2(s)}$ -like layer (Fig. S2). Similar TEM and XRD observations were made when surface precipitation of a  $\text{Fe}(\text{OH})_{2(s)}$ -like phase occurred onto magnetite nanoparticles.<sup>41</sup>

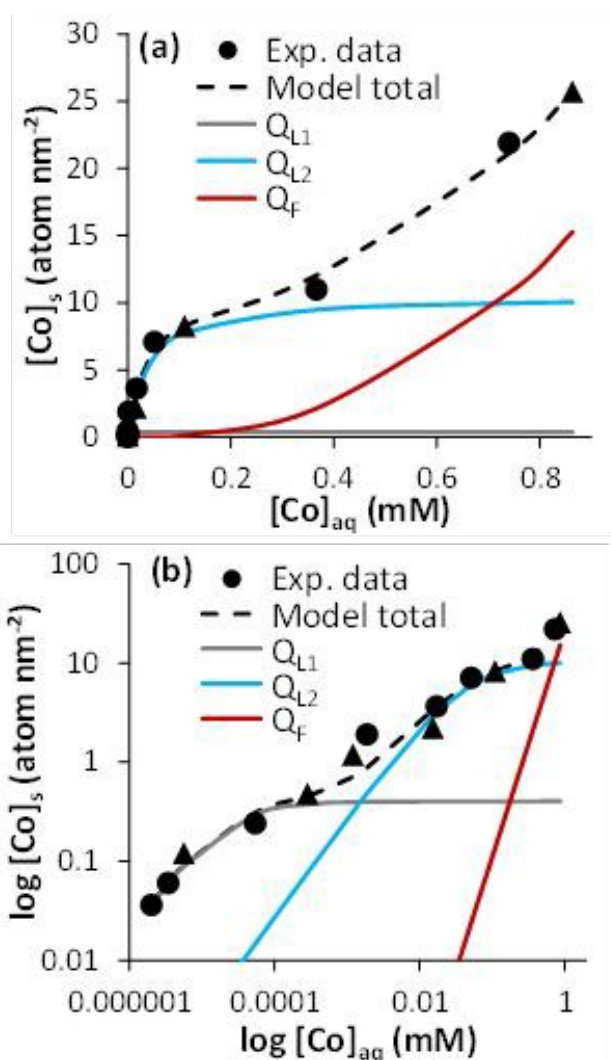


**Fig. 1.** Cobalt adsorption isotherm on magnetite ( $0.5 \text{ g L}^{-1}$ ), at pH 8 in 10 mM NaCl solution. Data are plotted on (a) linear and (b) logarithmic scales. Circles represent the experimental data ("exp. data"). Triangles correspond to the samples analyzed by XAS and XMCD. Dashed black lines are model results using a combination of two Langmuir ( $Q_{L1}$  and  $Q_{L2}$  as grey and blue lines, respectively) and one Freundlich isotherm equations ( $Q_F$ , red lines).

The use of a logarithm scale revealed an additional non-ideal sorption behavior of Co at low surface loadings (Fig. 1b), which can be associated to at least two Co-magnetite binding processes: a strong Co-magnetite binding for approximately  $[\text{Co}]_s \leq 1$  atom  $\text{nm}^{-2}$ , and a weaker one for  $1 \leq [\text{Co}]_s \leq 10$  atom  $\text{nm}^{-2}$ . Accordingly, sorption isotherm modeling was performed

assuming three mechanisms respectively described by two Langmuir equations (L1 and L2) to account for Co-magnetite binding up to the sorption plateau, and one Freundlich equation (F), to account for Co surface precipitation:

$$[Co]_s = Q_{L1} + Q_{L2} + Q_F \quad (2)$$

In equation 2,  $Q_{L,i}$  ( $i = 1$  or  $2$ ) and  $Q_F$  are magnetite-bound Co amounts. Values of  $Q_{L,i}$  are calculated according to the Langmuir model:

$$Q_{L,i} = Q_{max,i} \frac{K_{L,i}[Co]_{aq}}{1 + K_{L,i}[Co]_{aq}} \quad (3)$$

where  $Q_{max,i}$  is the adsorption capacities (here, in atom  $nm^{-2}$ ) and  $K_{L,i}$  are the Langmuir constants (in  $L \text{ mmol}^{-1}$ ). Values of  $Q_F$  are calculated using the following equation:

$$Q_F = K_F [Co]_{aq}^n \quad (4)$$

where  $K_F$  is the Freundlich constant, and  $n$  is the non-ideality parameter. Parameters of equation 2 were optimized using a least square fitting procedure (Table S2). The results of the fit are shown in Fig. 1a,b, in which the experimental results are well predicted by the model combining the three adsorption isotherm models. Values of  $Q_{max,i}$  are  $0.45 \pm 0.13$  and  $10.09 \pm 1.70$  atom  $nm^{-2}$ , for the  $L_1$  and  $L_2$  models respectively (Table S2). Even though this model is simple, as it does not account, for instance, for the potential Co-oligomer formation or electrostatic effects discussed above, it provides further evidence for the formation of at least three distinct surface species and a semi-quantitative guide for the interpretation of the isotherm data and, later in this manuscript, spectroscopic ones.

### 3.2. Cobalt surface speciation analysis by XAS and XMCD

XAS and XMCD analysis were performed to investigate the speciation of magnetite-bound Co. Fig. 2a shows isotropic XAS at the Co  $L_3$ -edge for different Co surface loadings depicted as triangles in the isotherm plots (Fig.1;  $0.12 \leq [Co]_s \leq 25.74$  atom  $nm^{-2}$ ). Full range spectra at the Co  $L_{2,3}$ -edges are also shown in Fig. S3a. All spectra exhibit four contributions at 772 eV (peak A), 773.4 eV (peak B), 773.8 eV (peak C) and 774.7 eV (peak D). These peaks correspond to  $Co^{2+}$  multiplets, i.e., the different possible energy transitions due to important interactions between the valence electrons and the electrons close to the nucleus.<sup>72</sup> All spectra were normalized to peak C, in order to deduce qualitative information on the structure of the Co at the surface of the  $Fe_3O_4$  nanoparticles from the evolution of the relative intensity of the other peaks (A, B, and D). Results were also compared with spectra of  $CoFe_2O_4$  (taken from Sartori



*et al.* 2019)<sup>26</sup> and  $\beta$ -Co(OH)<sub>2(s)</sub> (see the XRD pattern in Fig. S2). At low cobalt concentrations, spectra exhibit a more intense peak C relative to the other peaks. These spectra are similar to those recorded for adsorbed molecular complexes of Co<sup>2+</sup> onto magnetite, either via the Co<sup>2+</sup> ion<sup>7</sup> or the ligand,<sup>73</sup> or CoFe<sub>2</sub>O<sub>4</sub> (Fig. 2a). This suggests that, at low concentrations, Co<sup>2+</sup> either incorporates into magnetite or adsorbs onto its surface, the XAS signal being similar for these chemical species. However, at any [Co]<sub>s</sub> investigated, analysis at the Fe L<sub>2,3</sub>-edges XAS and XMCD show no detectable effect of Co on Fe stoichiometry (Fig. S4), which suggests no significant substitution of Fe by Co in the Fe<sub>3</sub>O<sub>4</sub> structure, and might point to the prevalence of adsorbed Co ions compared to incorporated Co. Diffusion is a temperature-dependent phenomenon and Co<sup>2+</sup> diffusion in magnetite crystal lattice has only been observed at high temperatures, often with substitution of Fe<sup>2+</sup> atoms.<sup>74–77</sup> When [Co]<sub>s</sub> increases, the intensity increase of peaks A, B and D confirms the presence of a Co(OH)<sub>2(s)</sub>-like phase,<sup>78,79</sup> in agreement with isotherm data and TEM images (Fig. S1).

Linear combination analyses of normalized Co L<sub>3</sub>-edge XAS spectra (from 770 to 780 eV) were performed to determine Co surface speciation versus Co surface loading (Fig. S5). Because only two species were distinguished by XAS, spectra of Co(OH)<sub>2(s)</sub> and CoFe<sub>2</sub>O<sub>4</sub> were used for the linear combination fit (LCF). The percentage of the Co(OH)<sub>2(s)</sub>-like phase determined by LCF is plotted against [Co]<sub>s</sub> in Fig. 2b. These data are compared with surface speciation modeling results, assuming the precipitation of the Co(OH)<sub>2(s)</sub>-like phase to be described by the Freundlich equation (eq. 2 and 4). Both approaches qualitatively agree with the increasing amount of Co(OH)<sub>2(s)</sub> with increasing [Co]<sub>s</sub> and with the absence of Co(OH)<sub>2(s)</sub> for [Co]<sub>tot</sub> < 1.19 atom nm<sup>-2</sup>. According to isotherm modeling, the amount of the Co(OH)<sub>2(s)</sub>-like phase remains below 2% up to Co<sub>s</sub> concentrations equal to ca. 8.30 atom nm<sup>-2</sup>. By contrast, linear combinations of XAS data show an increase in the fraction of Co(OH)<sub>2(s)</sub> from 0 to 24% between [Co]<sub>s</sub> = 0.48 and 8.30 atom nm<sup>-2</sup>. This occurs in conditions similar to the sorption plateau, where Co-oligomers were suspected to form, and might indicate that XAS signal is affected by the formation of such surface species. This difference can also be attributed to the fact that the linear combinations of XAS allows to differentiate only two species while the adsorption isotherm allows to distinguish three species.



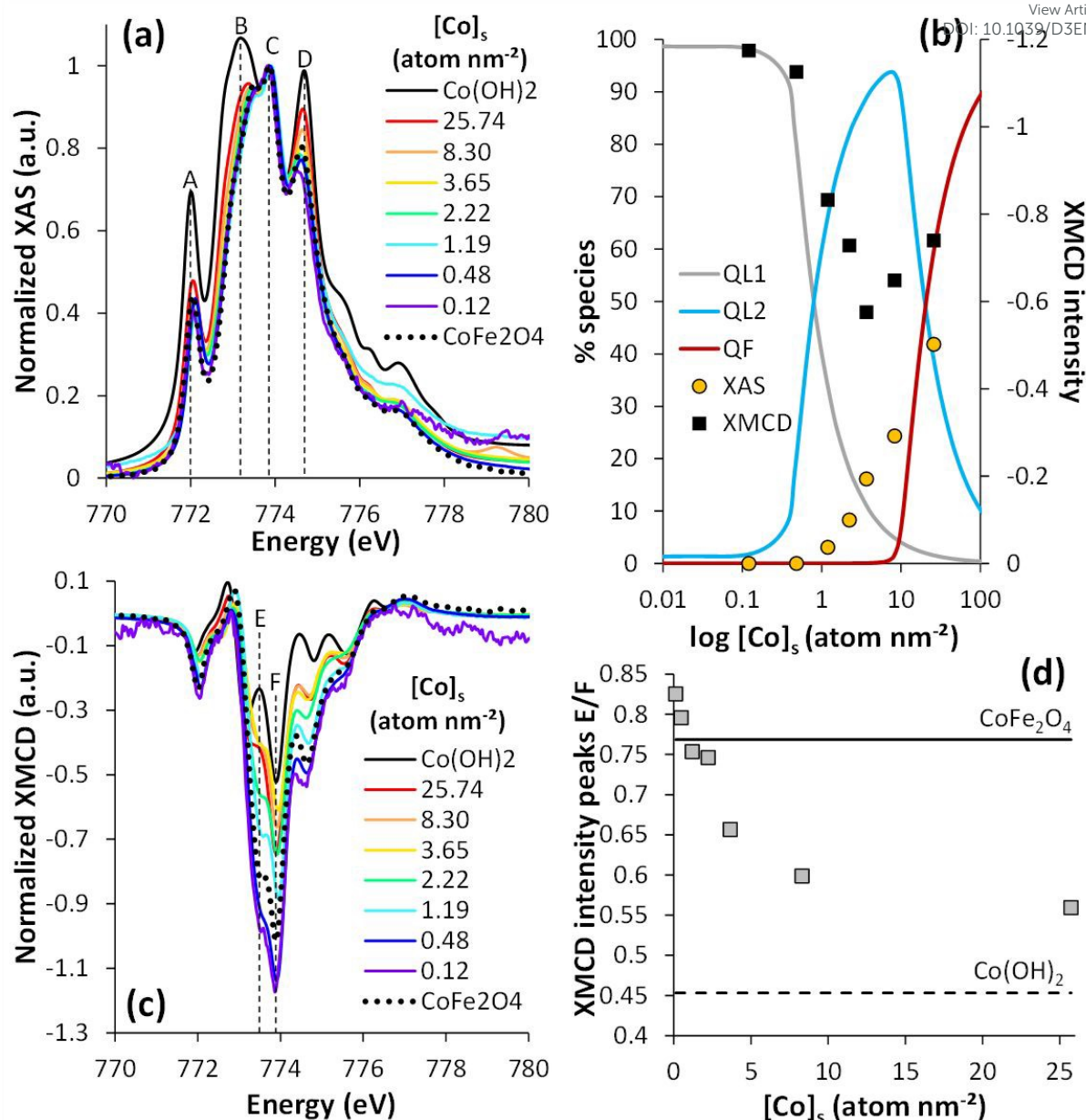


**Fig. 2.** Normalized XAS (a) and XMCD (c) spectra at the Co  $L_3$ -edge (see  $L_{2,3}$ -edges in Fig. S3) of stoichiometric magnetite with different Co surface loadings ( $0.12 \leq [\text{Co}]_s \leq 25.74$  atom  $\text{nm}^{-2}$ ). XAS and XMCD signals are normalized by dividing the raw signal by the maximum XAS peak. (b) The percentage of the different species identified using the adsorption isotherm equation 2 versus Co surface loading, are compared to the percentage of  $\text{Co}(\text{OH})_{2(s)}$ -like phase calculated from LCF of XAS data (yellow points) and, on the secondary axis, the XMCD intensity (black squares). (d) XMCD intensity ratio of E and F peaks, as a function of  $[\text{Co}]_s$ . The dotted line corresponds to the XMCD intensity of  $\text{Co}(\text{OH})_{2(s)}$  and the solid line to  $\text{CoFe}_2\text{O}_4$  references.

Corresponding normalized XMCD spectra are shown in Fig. 2c, at Co  $L_3$ -edge (see Fig. S3b for the Co  $L_2$ -edge). The spectra are typical of  $\text{Co}^{2+}$ .<sup>7,59,73,80–82</sup> The negative XMCD intensity values correspond to Co in octahedral environment.<sup>26,81,83</sup> All spectra exhibit several peaks, related to  $\text{Co}^{2+}$  multiplets, especially a major peak at 773.9 eV (denoted peak F) and its shoulder at approximately 773.5 eV (denoted peak E). XMCD signal is largest for low  $[\text{Co}]_s$  (0.12 and 0.48 atom  $\text{nm}^{-2}$ ), and the spectra are very similar to that of  $\text{CoFe}_2\text{O}_4$  nanoparticles

or adsorbed molecular Co complexes,<sup>59,84,85</sup> both compounds showing similar XMCD signals (like for XAS).<sup>7,73</sup>

The intensity of peak F exceeds 1 which can be attributed to surface spin canting effects.<sup>26,86</sup> The XMCD signal decreases with increasing  $[\text{Co}]_s$  from 0.48 to 3.65 atom  $\text{nm}^{-2}$ , before increasing with  $[\text{Co}]_s > 3.65$  atom  $\text{nm}^{-2}$ . In addition, the energy of the peak shoulder E shifts to lower values with increasing  $[\text{Co}]_s$  (from 773.5 eV to 773.2 eV, between  $[\text{Co}]_s = 0.12$  to 25.74 atom  $\text{nm}^{-2}$ ), which is accompanied by a decrease of its intensity with respect to that of peak F (Fig. 2d). The observations at intermediate  $[\text{Co}]_s$  suggest the occurrence of a species with a weak magnetic signal, whereas data at large  $[\text{Co}]_s$  are in line with the formation of the  $\text{Co}(\text{OH})_{2(s)}$ -like precipitate. The XMCD spectrum of  $\text{Co}(\text{OH})_{2(s)}$  exhibits a smaller signal than  $\text{CoFe}_2\text{O}_4$  and more easily distinguishable peaks E (773.5 eV) from Fe.<sup>26</sup> In principle,  $\text{Co}(\text{OH})_{2(s)}$  should exhibit no XMCD signal, being antiferromagnetic, but the strong magnetic field applied for the present measurements ( $\pm 6$  T) may align part of the  $\text{Co}^{2+}$  spins of a non-crystalline  $\text{Co}(\text{OH})_{2(s)}$  phase.<sup>87–89</sup>

Suspected spin canting effects prevent the estimation of Co speciation by XMCD. Instead, the maximum peak intensity is qualitatively compared with the calculated speciation using the isotherm model (Fig. 2b). The disappearance of the first species, prevailing at low  $[\text{Co}]_s$ , corresponds rather well to the drop in the XMCD signal intensity. For large  $[\text{Co}]_s$ , the XMCD signal increase coincides with the increase in the amount of  $\text{Co}(\text{OH})_{2(s)}$ -like phase. These results suggest that the Co species with weak magnetic signal forms at intermediate surface loadings, which corresponds to the prevailing Co species when the sorption isotherm reaches a plateau (at around 10 atom  $\text{nm}^{-2}$ ). Altogether, wet chemical experiments, XAS and XMCD at Fe and Co  $L_3$ -edges point to the formation of (i) relatively strong Co surface complexes or incorporated Co species at low loadings ( $< 1$  atom  $\text{nm}^{-2}$ ), (ii) Co-oligomeric species formations with antiferromagnetically coupled spins, and (iii)  $\text{Co}(\text{OH})_{2(s)}$ -like surface precipitates.

### 3.3. Probing the cobalt speciation by XMCD magnetization curves

For metal oxide nanoparticles, the magnetic properties depend on the valence state of the 3d elements and the spin moments alignment of the cations in the crystalline structure. Therefore, following the magnetization curves at specific sites ( $\text{Co}^{2+}_{(\text{Oh})}$ ,  $\text{Fe}^{2+}$  and  $\text{Fe}^{3+}_{(\text{Oh})}$  and  $(\text{Td})$ ) give complementary information about the behavior of the adsorbed or incorporated Co on the magnetite surface. The saturation at high field, the remanent magnetization (at zero field) and the coercive field (at zero magnetization) allow to distinguish the Co-bearing phases at the magnetite surface. For four  $[\text{Co}]_s$ , ranging from 0.48 to 25.74 atom  $\text{nm}^{-2}$ , XMCD magnetization curves XMCD(H) were measured at a fixed energy (773.9 eV), and under a

magnetic field parallel to the beam varying from -6 to 6 T. XMCD (H) curves (Fig. 3) show different behavior depending on the Co surface loading. At 0.48 atom nm<sup>-2</sup>, the magnetization curve corresponds to a ferrimagnetic phase like a cobalt ferrite which is characterized by a relatively fast magnetic saturation and a coercive field. At highest Co concentration the magnetization curve corresponds to an antiferromagnetic phase that is characterized by a weaker saturation and highest coercive field. Following the magnetization curves versus the Co concentration, the saturation is faster for low Co concentrations and the coercive field is stronger for high concentrations. The saturation of the magnetization curves for samples with low Co concentration is attributed to Co<sup>2+</sup> in CoFe<sub>2</sub>O<sub>4</sub>-like magnetic structure, caused by the high magnetic moment of Co<sup>2+</sup>.<sup>26,90</sup> The low saturation for samples with high Co concentrations indicates the presence of antiferromagnetic phase superimposed to the ferrimagnetic phase already present at low concentration, causing a spin tilt in the surface layer on the magnetic particles and degrading the magnetic properties.<sup>90,91</sup> The magnetic signals of Fe are similar at different Co concentrations, except for the coercive field (Fig. S6). Coercive field (H<sub>c</sub>) and the remanence to saturation ratio (M<sub>r</sub>/M<sub>s</sub>) were measured at the Co and Fe edges (Table 1). Similar H<sub>c</sub> values calculated for high Co concentration at Fe and Co edges agree with strong exchange coupling of Co and Fe atoms.<sup>26,92,93</sup> The M<sub>r</sub>/M<sub>s</sub> values confirm that with increasing [Co]<sub>s</sub> the unsaturation increases. These results suggest that at low Co concentrations ([Co]<sub>s</sub> = 0.48 atom nm<sup>-2</sup>), a magnetically phase similar to CoFe<sub>2</sub>O<sub>4</sub> forms on the magnetite surface which agrees with the results obtained for the surface speciation that predicts the adsorption or incorporation of Co atoms onto the magnetite surface. The decrease in the coercive field for [Co]<sub>s</sub> = 2.22 atom nm<sup>-2</sup>, with saturation of magnetization, suggests a change in surface speciation with the formation of oligomers exhibiting weaker magnetic properties. When [Co]<sub>s</sub> = 8.3 atom nm<sup>-2</sup>, the coercive field increases again with a limitation of saturation, confirming the partial precipitation of Co(OH)<sub>2(s)</sub>-like phase onto magnetite. The coercive field continues to increase as [Co]<sub>s</sub> increases, again with unsaturation, demonstrating the formation of a Co(OH)<sub>2(s)</sub>-like layer, which leads to interesting magnetic properties with antiferromagnetic layer. These results are in excellent agreement with analysis from XAS and XMCD. The behavior of magnetization curves for high cobalt concentration suggests a hard magnet behavior, while for low cobalt concentration, the behavior tends to be a mixture of hard and soft magnets.<sup>82</sup>





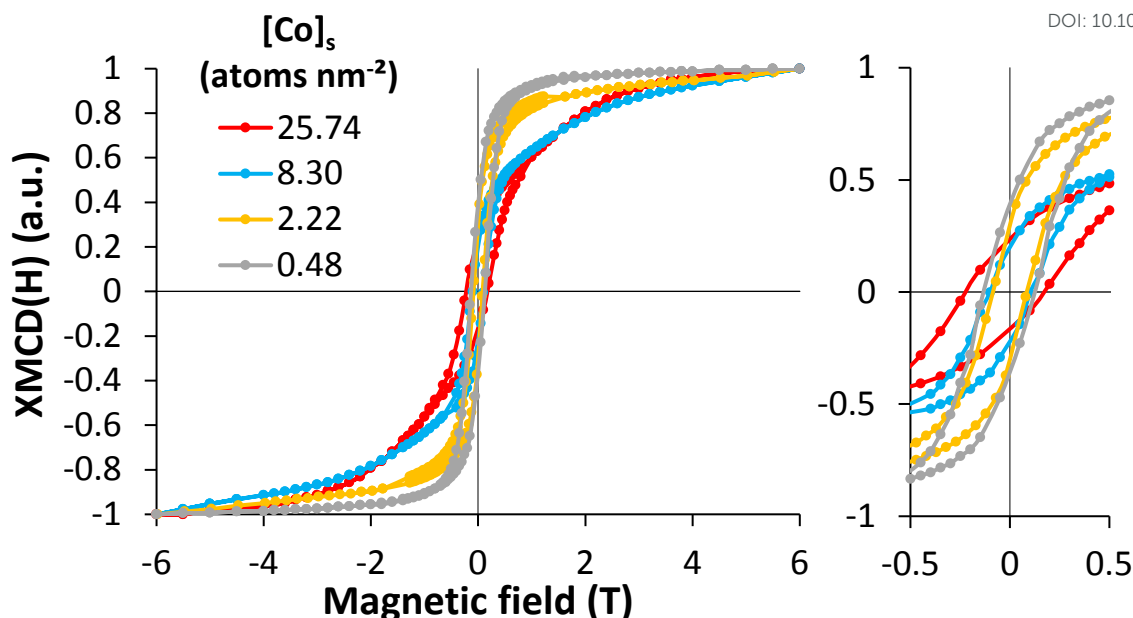


**Fig. 3** XMCD magnetization versus magnetic field measurement at Co  $L_3$ -edge at 4.2 K for four solid cobalt concentrations (from 0.48 to 25.74 atom  $\text{nm}^{-2}$ ). All curves are normalized to 1 in order to compare the magnetization behavior versus the  $[\text{Co}]_s$ . The raw XMCD magnetization curves can be seen in the SI (see Fig. S7).

**Table 1.** Coercive field and  $M_r/M_s$  values obtained for element specific hysteresis measured by XMCD on  $\text{Fe}_3\text{O}_4$  nanoparticles with different Co adsorption, with  $[\text{Co}]_s$  ranging from 0.48 to 25.74 atom  $\text{nm}^{-2}$ .  $H_c$ ,  $M_r$  and  $M_s$  are respectively the coercive field, the remanent magnetization and the magnetization at 6T.

| Sample       | $[\text{Co}]_s = 0.48$<br>$\text{nm}^{-2}$ | $[\text{Co}]_s = 2.22$<br>$\text{nm}^{-2}$ | $[\text{Co}]_s = 8.30$<br>$\text{nm}^{-2}$ | $[\text{Co}]_s = 25.74$<br>$\text{nm}^{-2}$ | $\text{Co}(\text{OH})_2$ |
|--------------|--|--|--|---|--------------------------|
| Hc Co        | 0.13                                       | 0.09                                       | 0.10                                       | 0.20  | 0.29                     |
| Hc Fe        | 0.10                                       | 0.03                                       | 0.10                                       | 0.19  |                          |
| $M_r/M_s$ Co | 0.37                                       | 0.30                                       | 0.21                                       | 0.20  | 0.09                     |
| $M_r/M_s$ Fe | 0.29                                       | 0.14                                       | 0.30                                       | 0.44  |                          |

#### 4. Conclusion

Magnetite nanoparticles have a strong affinity for  $\text{Co}^{2+}$ . Therefore, these nanoparticles have a high potential for environmental (decontamination) and electronic (core-shell structure) applications. Magnetite is already widely used in many fields but the understanding of its interactions with metals, and the resulting properties, is still limited. In this study, the mechanisms involved were investigated using magnetite nanoparticles  $\text{Co}^{2+}$  solution at different concentrations, under anaerobic conditions. The results obtained give a better understanding of the interactions between magnetite and Co, at the nanoscale. The characterization of the nanoparticles showed that the addition of Co does not modify the size of the nanoparticles, which is about 10 nm. However, magnetite nanoparticles with high Co concentrations show a gangue, about 1 to 1.5 nm thick, constituted of amorphous Co hydroxide. Modeling of adsorption isotherms gives rise to three different behavior as a function

of Co concentrations: (i) adsorption or incorporation of Co-monomers on magnetite, with strong bonds, at low concentrations, (ii) adsorption of Co ions as oligomers at intermediate concentrations, with weaker bonds, and (iii) precipitation of Co ions at high concentrations. XMCD analyses and magnetization curves allowed to define the magnetic properties of magnetite-Co nanoparticles. The three surface species show different magnetic properties. The Co-monomers have a magnetic behavior similar to that of  $\text{CoFe}_2\text{O}_4$  particles, with the formation of a ferrimagnetic phase, while the Co-precipitate has a behavior close to that of  $\text{Co(OH)}_{2(s)}$  particles, which forms a core-shell structure, with the formation of an antiferromagnetic phase. On the other hand, the Co-oligomers have diminished magnetic properties. This study has a double interest. First, these results provide a comprehensive view of Co speciation, which can be useful for environmental applications, including soil and water remediation. Secondly, it provides a better understanding of the magnetic behavior of magnetite-Co nanoparticles, according to speciation, which allow to predict the magnetic properties and to adapt magnetite-Co synthesis for electronic applications.

### Author contributions

Laura Fablet: writing-original draft, data curation, investigation, visualization.

Mathieu Pédrot: writing – review & editing, resources, supervision, project administration, funding acquisition

Fadi Choueikani: writing – review & editing, resources, supervision, project administration, funding acquisition

Margaux Kerdiles: investigation, data curation

Mathieu Pasturel: investigation, data curation, writing – review & editing

Rémi Marsac: writing – review & editing, resources, supervision, project administration, funding acquisition

### Conflicts of interest

There are no conflicts to declare.

### Acknowledgments

This work was supported by the French Brittany Region (ARED project "NANOMAG"), SOLEIL synchrotron, the C-FACTOR project funded by ANR (project number ANR-18-CE01-0008) and the SURFNANO project funded by the CNRS-INSU EC2CO program. Through the support of the GeOHeLiS analytical platform of Rennes University, this publication is also supported by the European Union through the European Regional Development Fund (FEDER), the French Ministry of Higher Education and Research, the French Region of Brittany and Rennes Metropole. The authors further acknowledge the SOLEIL synchrotron for beamtime allocation at the DEIMOS beamline (proposal no. 20210864). The authors are grateful to M. Bouhnik-Le Coz and M. Pattier for assistance in ICP-MS and UV-vis analysis, as well as V. Dorcet and L. Rault for assistance in TEM experiments performed on the THEMIS platform (ScanMAT, UMS 2011 University of Rennes-CNRS; CPER-FEDER 2007–2014).

## References

- 1 J. L. Gould, The Case for Magnetic Sensitivity in Birds and Bees (Such As It Is): Surprising concentrations of magnetite in the tissues of some animals may explain their sensitivity to the earth's magnetic field, *Am. Sci.*, 1980, **68**, 256–267.
- 2 R. B. Frankel, Magnetic Guidance Of Organisms, *Annu. Rev. Biophys. Bioeng.*, 1984, 85–103.
- 3 R. M. Cornell and U. Schwertmann, *The Iron Oxides: Structure, Properties, Reactions, Occurrences and Uses*, Wiley-VCH: Berlin, 1st edn., 2003.
- 4 G. J. Churchman and D. J. Lowe, *Alteration, Formation, and Occurrence of Minerals in Soils*, CRC Press, 2012.
- 5 J. M. Byrne, N. Klueglein, C. Pearce, K. M. Rosso, E. Appel and A. Kappler, Redox cycling of Fe(II) and Fe(III) in magnetite by Fe-metabolizing bacteria, *Science*, 2015, **347**, 1473–1476.
- 6 P. Majewski and B. Thierry, Functionalized Magnetite Nanoparticles—Synthesis, Properties, and Bio-Applications, *Crit. Rev. Solid State Mater.*, 2007, **32**, 203–215.
- 7 Y. Prado, N. Daffé, A. Michel, T. Georgelin, N. Yaacoub, J.-M. Grenèche, F. Choueikani, E. Otero, P. Ohresser, M.-A. Arrio, C. Cartier-dit-Moulin, P. Sainctavit, B. Fleury, V. Dupuis, L. Lisnard and J. Fresnais, Enhancing the magnetic anisotropy of maghemite nanoparticles via the surface coordination of molecular complexes, *Nat. Commun.*, 2015, **6**, 1–8.
- 8 M. Usman, J. M. Byrne, A. Chaudhary, S. Orsetti, K. Hanna, C. Ruby, A. Kappler and S. B. Haderlein, Magnetite and Green Rust: Synthesis, Properties, and Environmental Applications of Mixed-Valent Iron Minerals, *Chem. Rev.*, 2018, **118**, 3251–3304.
- 9 S. Fang, D. Bresser and S. Passerini, Transition Metal Oxide Anodes for Electrochemical Energy Storage in Lithium- and Sodium-Ion Batteries, *Adv. Energy Mater.*, 2020, **10**, 1902485.
- 10 D. H. Lindsley, Experimental studies of oxide minerals, *Rev. Mineral. Geochem.*, 1991, **25**, 69–106.

- 11 F. N. Skomurski, S. Kerisit and K. M. Rosso, Structure, charge distribution, and electron hopping dynamics in magnetite (Fe<sub>3</sub>O<sub>4</sub>) (100) surfaces from first principles, *Geochim. Cosmochim. Acta*, 2010, **74**, 4234–4248.
- 12 C. A. Gorski, J. Nurmi, P. Tratnyek, T. Hofstetter and M. M. Scherer, Redox Behavior of Magnetite: Implications for Contaminant Reduction, *Environ. Sci. Technol.*, 2010, **44**, 55–60.
- 13 D. E. Latta, C. A. Gorski, M. I. Boyanov, E. J. O’Loughlin, K. M. Kemner and M. M. Scherer, Influence of Magnetite Stoichiometry on UVI Reduction, *Environ. Sci. Technol.*, 2012, **46**, 778–786.
- 14 C. J. Goss, Saturation magnetisation, coercivity and lattice parameter changes in the system Fe<sub>3</sub>O<sub>4</sub>- $\gamma$ -Fe<sub>2</sub>O<sub>3</sub>, and their relationship to structure, *Phys. Chem. Minerals*, 1988, **16**, 164–171.
- 15 G. F. Goya, T. S. Berquó, F. C. Fonseca and M. P. Morales, Static and dynamic magnetic properties of spherical magnetite nanoparticles, *J. Appl. Phys.*, 2003, **94**, 3520–3528.
- 16 A. S. Teja and P.-Y. Koh, Synthesis, properties, and applications of magnetic iron oxide nanoparticles, *Prog. Cryst. Growth Charact. Mater.*, 2009, **55**, 22–45.
- 17 M. Auffan, J. Rose, J.-Y. Bottero, G. V. Lowry, J.-P. Jolivet and M. R. Wiesner, Towards a definition of inorganic nanoparticles from an environmental, health and safety perspective, *Nat. Nanotechnol.*, 2009, **4**, 634–641.
- 18 B. Issa, I. M. Obaidat, B. A. Albiss and Y. Haik, Magnetic Nanoparticles: Surface Effects and Properties Related to Biomedicine Applications, *Int. J. Mol. Sci.*, 2013, **14**, 21266–21305.
- 19 Y. Zhu, X. Zhang, K. Koh, L. Kovarik, J. L. Fulton, K. M. Rosso and O. Y. Gutiérrez, Inverse iron oxide/metal catalysts from galvanic replacement, *Nat. Commun.*, 2020, **11**, 3269.
- 20 A. Ito, M. Shinkai, H. Honda and T. Kobayashi, Medical application of functionalized magnetic nanoparticles, *J. Biosci. Bioeng.*, 2005, **100**, 1–11.
- 21 M. Liu, C. Chen, J. Hu, X. Wu and X. Wang, Synthesis of Magnetite/Graphene Oxide Composite and Application for Cobalt(II) Removal, *J. Phys. Chem. C*, 2011, **115**, 25234–25240.
- 22 S. Tizro and H. Baseri, Removal of Cobalt Ions from Contaminated Water Using Magnetite Based Nanocomposites: Effects of Various Parameters on the Removal Efficiency, *J. Water Environ. Nanotechnol.*, 2017, **2**, 174–185.
- 23 C. Das, S. Sen, T. Singh, T. Ghosh, S. S. Paul, T. W. Kim, S. Jeon, D. K. Maiti, J. Im and G. Biswas, Green Synthesis, Characterization and Application of Natural Product Coated Magnetite Nanoparticles for Wastewater Treatment, *Nanomaterials*, 2020, **10**, 1615.
- 24 H. Zhang, Y. Liu and S. Sun, Synthesis and assembly of magnetic nanoparticles for information and energy storage applications, *Front. Phys. China*, 2010, **5**, 347–356.
- 25 Q. Song and Z. J. Zhang, Controlled Synthesis and Magnetic Properties of Bimagnetic Spinel Ferrite CoFe<sub>2</sub>O<sub>4</sub> and MnFe<sub>2</sub>O<sub>4</sub> Nanocrystals with Core–Shell Architecture, *J. Am. Chem. Soc.*, 2012, **134**, 10182–10190.
- 26 K. Sartori, G. Cotin, C. Bouillet, V. Halté, S. Bégin-Colin, F. Choueikani and B. P. Pichon, Strong interfacial coupling through exchange interactions in soft/hard core–shell nanoparticles as a function of cationic distribution, *Nanoscale*, 2019, **11**, 12946–12958.
- 27 F. Choueikani, F. Royer, D. Jamon, A. Siblino, J. J. Rousseau, S. Neveu and J. Charara, Magneto-optical waveguides made of cobalt ferrite nanoparticles embedded in silica/zirconia organic-inorganic matrix, *Appl. Phys. Lett.*, 2009, **94**, 051113.
- 28 H. Amata, F. Royer, F. Choueikani, D. Jamon, F. Parsy, J.-E. Broquin, S. Neveu and J. Jacques Rousseau, Hybrid magneto-optical mode converter made with a magnetic

- nanoparticles-doped SiO<sub>2</sub>/ZrO<sub>2</sub> layer coated on an ion-exchanged glass waveguide, *Appl. Phys. Lett.*, 2011, **99**, 251108.
- 29 M. Sugimoto, The Past, Present, and Future of Ferrites, *J. Am. Chem. Soc.*, 1999, **82**, 269–280.
- 30 S. Staniland, W. Williams, N. Telling, G. Van Der Laan, A. Harrison and B. Ward, Controlled cobalt doping of magnetosomes in vivo, *Nat. Nanotechnol.*, 2008, **3**, 158–162.
- 31 B. Babukutty, N. Kalarikkal and S. S. Nair, Studies on structural, optical and magnetic properties of cobalt substituted magnetite fluids (CoFe<sub>1-x</sub>Fe<sub>2</sub>O<sub>4</sub>), *Mater. Res. Express*, 2017, **4**, 035906.
- 32 S. P. Gubin, Y. I. Spichkin, G. Y. Yurkov and A. M. Tishin, Nanomaterial for High-Density Magnetic Data Storage, *Russ. J. Inorg. Chem.*, 2002, **47**, 32–67.
- 33 F. Choueikani, D. Jamon, S. Neveu, M.-F. Blanc-Mignon, Y. Lefkir and F. Royer, Self-biased magneto-optical films based on CoFe<sub>2</sub>O<sub>4</sub>–silica nanocomposite, *Journal of Applied Physics*, 2021, **129**, 023101.
- 34 T. Missana, C. Maffiotte and M. García-Gutiérrez, Surface reactions kinetics between nanocrystalline magnetite and uranyl, *J. Colloid Interface Sci.*, 2003, **261**, 154–160.
- 35 J.-W. Moon, Y. Roh, R. J. Lauf, H. Vali, L. W. Yeary and T. J. Phelps, Microbial preparation of metal-substituted magnetite nanoparticles, *J. Microbiol. Methods*, 2007, **70**, 150–158.
- 36 R. Bliem, J. Pavelec, O. Gamba, E. McDermott, Z. Wang, S. Gerhold, M. Wagner, J. Osiecki, K. Schulte, M. Schmid, P. Blaha, U. Diebold and G. S. Parkinson, Adsorption and incorporation of transition metals at the magnetite Fe<sub>3</sub>O<sub>4</sub> (001) surface, *Phys. Rev. B*, 2015, **92**, 075440.
- 37 T. Gaudisson, R. Sayed-Hassan, N. Yaacoub, G. Franceschin, S. Nowak, J.-M. Grenèche, N. Menguy, P. Saintavit and S. Ammar, On the exact crystal structure of exchange-biased Fe<sub>3</sub>O<sub>4</sub>–CoO nanoaggregates produced by seed-mediated growth in polyol, *CrystEngComm*, 2016, **18**, 3799–3807.
- 38 L. Giraldo, A. Erto and J. C. Moreno-Piraján, Magnetite nanoparticles for removal of heavy metals from aqueous solutions: synthesis and characterization, *Adsorption*, 2013, **19**, 465–474.
- 39 H. Catalette, J. Dumonceau and P. Ollar, Sorption of cesium, barium and europium on magnetite, *J. Contam. Hydrol.*, 1998, **35**, 151–159.
- 40 G. S. Parkinson, Iron oxide surfaces, *Surf. Sci. Rep.*, 2016, **71**, 272–365.
- 41 P. Jungcharoen, M. Pédrot, F. Choueikani, M. Pasturel, K. Hanna, F. Heberling, M. Tesfa and R. Marsac, Probing the effects of redox conditions and dissolved Fe<sup>2+</sup> on nanomagnetite stoichiometry by wet chemistry, XRD, XAS and XMCD, *Environ. Sci.: Nano*, 2021, **8**, 2098–2107.
- 42 P. Jungcharoen, M. Pédrot, F. Heberling, K. Hanna, F. Choueikani, C. Catrouillet, A. Dia and R. Marsac, Prediction of nanomagnetite stoichiometry (Fe(II)/Fe(III)) under contrasting pH and redox conditions, *Environ. Sci.: Nano*, 2022, **9**, 2363–2371.
- 43 R. Marsac, M. Pasturel and K. Hanna, Reduction Kinetics of Nitroaromatic Compounds by Titanium-Substituted Magnetite, *J. Phys. Chem. C*, 2017, **121**, 11399–11406.
- 44 H. Tamura, N. Katayama and R. Furuichi, The Co<sup>2+</sup> Adsorption Properties of Al<sub>2</sub>O<sub>3</sub>, Fe<sub>2</sub>O<sub>3</sub>, Fe<sub>3</sub>O<sub>4</sub>, TiO<sub>2</sub>, and MnO<sub>2</sub> Evaluated by Modeling with the Frumkin Isotherm, *J. Colloid Interface Sci.*, 1997, **195**, 192–202.
- 45 A. Motl, F. Šebesta, J. D. Navratil and J. Hlavicova, Sorption of cobalt on magnetite, *Czechoslov. J. Phys.*, 2003, **53**, 515–523.

- 46 S. Hashemian, H. Saffari and S. Ragabion, Adsorption of Cobalt(II) from Aqueous Solutions by Fe<sub>3</sub>O<sub>4</sub>/Bentonite Nanocomposite, *Water Air Soil Pollut.*, 2015, **226**, 2212. View Article Online  
DOI: 10.1059/ESN00379E
- 47 N. Efimova, A. Krasnopyorova, G. Yuhno, D. S. Sofronov and M. Rucki, Uptake of Radionuclides <sup>60</sup>Co, <sup>137</sup>Cs, and <sup>90</sup>Sr with α-Fe<sub>2</sub>O<sub>3</sub> and Fe<sub>3</sub>O<sub>4</sub> Particles from Aqueous Environment, *Materials*, 2021, **14**, 2899.
- 48 W. Cheng, R. Marsac and K. Hanna, Influence of Magnetite Stoichiometry on the Binding of Emerging Organic Contaminants, *Environ. Sci. Technol.*, 2018, **52**, 467–473.
- 49 J. Deng, S. Bae, S. Yoon, M. Pasturel, R. Marsac and K. Hanna, Adsorption capacity of the corrosion products of nanoscale zerovalent iron for emerging contaminants, *Environ. Sci.: Nano*, 2020, **7**, 3773–3782.
- 50 R. Massart, Preparation of aqueous magnetic liquids in alkaline and acidic media, *IEEE Trans. Magn.*, 1981, **17**, 1247–1248.
- 51 E. Demangeat, M. Pédrot, A. Dia, M. Bouhnik-le-Coz, F. Grasset, K. Hanna, M. Kamagate and F. Cabello-Hurtado, Colloidal and chemical stabilities of iron oxide nanoparticles in aqueous solutions: the interplay of structural, chemical and environmental drivers, *Environ. Sci.: Nano*, 2018, **5**, 992–1001.
- 52 W. B. Fortune and M. G. Mellon, Determination of Iron with o-Phenanthroline: A Spectrophotometric Study, *Ind. Eng. Chem. Anal. Ed.*, 1938, **10**, 60–64.
- 53 H. Tamura, K. Goto, T. Yotsuyanagi and M. Nagayama, Spectrophotometric determination of iron(II) with 1,10-phenanthroline in the presence of large amounts of iron(III), *Talanta*, 1974, **21**, 314–318.
- 54 H. S. V. Klooster, Nitroso R-salt, a new reagent for the detection of cobalt, *J. Am. Chem. Soc.*, 1921, **43**, 746–749.
- 55 K. O. Zahir and H. Keshtkar, A Colorimetric Method for Trace Level Determination of Cobalt in Natural and Waste Water Samples, *Int. J. Environ. Anal. Chem.*, 1998, **72**, 151–162.
- 56 S. Zaheri, Thesis, Dept. of Materials Engineering, 2015.
- 57 D. Yeghicheyan, D. Aubert, M. Bouhnik-Le Coz, J. Chmeleff, S. Delpoux, I. Djouaev, G. Granier, F. Lacan, J.-L. Piro, T. Rousseau, C. Cloquet, A. Marquet, C. Menniti, C. Pradoux, R. Freyrier, E. Vieira da Silva-Filho and K. Suchorski, A New Interlaboratory Characterisation of Silicon, Rare Earth Elements and Twenty-Two Other Trace Element Concentrations in the Natural River Water Certified Reference Material SLRS-6 (NRC-CNRC), *Geostand. Geoanalytical Res.*, 2019, **43**, 475–496.
- 58 P. Ohresser, E. Otero, F. Choueikani, K. Chen, S. Stanescu, F. Deschamps, T. Moreno, F. Polack, B. Lagarde, J.-P. Daguette, F. Marteau, F. Scheurer, L. Joly, J.-P. Kappler, B. Muller, O. Bunau and Ph. Sainctavit, DEIMOS: A beamline dedicated to dichroism measurements in the 350–2500 eV energy range, *Review of Scientific Instruments*, 2014, **85**, 013106.
- 59 N. Daffé, F. Choueikani, S. Neveu, M.-A. Arrio, A. Juhin, P. Ohresser, V. Dupuis and P. Sainctavit, Magnetic anisotropies and cationic distribution in CoFe<sub>2</sub>O<sub>4</sub> nanoparticles prepared by co-precipitation route: Influence of particle size and stoichiometry, *J. Magn. Mater.*, 2018, **460**, 243–252.
- 60 D. L. Parkhurst and C. A. J. Appelo, User's guide to PHREEQC (Version 2): A computer program for speciation, batch-reaction, one-dimensional transport, and inverse geochemical calculations, *Water Resour. Invest. Rep.*, 1999, 99–4259.
- 61 N. Morelová, N. Finck, J. Lützenkirchen, D. Schild, K. Dardenne and H. Geckeis, Sorption of americium / europium onto magnetite under saline conditions: Batch experiments, surface complexation modelling and X-ray absorption spectroscopy study, *J. Colloid Interface Sci.*, 2020, **561**, 708–718.

- 62 M. Ponthieu, F. Juillot, T. Hiemstra, W. H. van Riemsdijk and M. F. Benedetti, Metal ion binding to iron oxides, *Geochim. Cosmochim. Acta*, 2006, **70**, 2679–2698.
- 63 J. C. Mendez and T. Hiemstra, High and low affinity sites of ferrihydrite for metal ion adsorption: Data and modeling of the alkaline-earth ions Be, Mg, Ca, Sr, Ba, and Ra, *Geochim. Cosmochim. Acta*, 2020, **286**, 289–305.
- 64 L. Weng, W. H. Van Riemsdijk and T. Hiemstra, Cu<sup>2+</sup> and Ca<sup>2+</sup> adsorption to goethite in the presence of fulvic acids, *Geochim. Cosmochim. Acta*, 2008, **72**, 5857–5870.
- 65 I. M. Ugwu and D. M. Sherman, Irreversibility of sorption of cobalt to goethite ( $\alpha$ -FeOOH) and disparities in dissolution of aged synthetic Co-goethite, *Chem. Geol.*, 2017, **467**, 168–176.
- 66 W. Cheng, E. L. Kalahroodi, R. Marsac and K. Hanna, Adsorption of Quinolone Antibiotics to Goethite under Seawater Conditions: Application of a Surface Complexation Model, *Environ. Sci. Technol.*, 2019, **53**, 1130–1138.
- 67 M. A. Blesa, R. M. Larotonda, A. J. G. Maroto and A. E. Regazzoni, Behavior of cobalt(II) in aqueous suspensions of magnetite, *Colloids Surf.*, 1982, **5**, 197–207.
- 68 K. J. Farley, D. A. Dzombak and F. M. M. Morel, A surface precipitation model for the sorption of cations on metal oxides, *J. Colloid Interface Sci.*, 1985, **106**, 226–242.
- 69 J. Lutzenkirchen and Ph. Behra, On the surface precipitation model for cation sorption at the (hydr)oxide water interface, *Aquat. Geochem.*, 1996, **1**, 375–397.
- 70 T. M. Petrova, L. Fachikov and J. Hristov, The magnetite as adsorbent for some hazardous species from aqueous solutions: a review, *Int. Rev. Chem. Eng.*, 2011, **3**, 19.
- 71 D. A. Dzombak and F. M. M. Morel, *Surface Complexation Modeling: Hydrous Ferric Oxide*, John Wiley & Sons, 1991.
- 72 M. W. Haverkort, Spin and orbital degrees of freedom in transition metal oxides and oxide thin films studied by soft x-ray absorption spectroscopy, Thesis, University Koeln, 2005.
- 73 V. E. Campbell, M. Tonelli, I. Cimatti, J.-B. Moussy, L. Tortech, Y. J. Dappe, E. Rivière, R. Guillot, S. Delprat, R. Mattana, P. Seneor, P. Ohresser, F. Choueikani, E. Otero, F. Koprowiak, V. G. Chilkuri, N. Suaud, N. Guihéry, A. Galtayries, F. Miserque, M.-A. Arrio, P. Saintavit and T. Mallah, Engineering the magnetic coupling and anisotropy at the molecule–magnetic surface interface in molecular spintronic devices, *Nat. Commun.*, 2016, **7**, 13646.
- 74 M. Sharrock, P. Picone and A. Morrish, Mössbauer emission spectroscopy study of cobalt-surface-doped acicular magnetite particles, *IEEE Trans. Magn.*, 1983, **19**, 1466–1473.
- 75 P. Auric, G. M. Chen, H. L. Luo, D. Y. Yang and K. Sun, Mössbauer experiments on cobalt-ferrite epitaxial magnetite, *J. Magn. Magn. Mater.*, 1988, **72**, 319–329.
- 76 J. Toth, *Adsorption*, CRC Press, 2002.
- 77 G. Franceschin, T. Gaudisson, N. Menguy, B. C. Dodrill, N. Yaacoub, J.-M. Grenèche, R. Valenzuela and S. Ammar, Exchange-Biased Fe<sub>3</sub>-xO<sub>4</sub>-CoO Granular Composites of Different Morphologies Prepared by Seed-Mediated Growth in Polyol: From Core–Shell to Multicore Embedded Structures, *Part. Part. Syst. Charact.*, 2018, **35**, 1800104.
- 78 S. Ya. Istomin, O. A. Tyablikov, S. M. Kazakov, E. V. Antipov, A. I. Kurbakov, A. A. Tsirlin, N. Hollmann, Y. Y. Chin, H.-J. Lin, C. T. Chen, A. Tanaka, L. H. Tjeng and Z. Hu, An unusual high-spin ground state of Co<sup>3+</sup> in octahedral coordination in brownmillerite-type cobalt oxide, *Dalton Transactions*, 2015, **44**, 10708–10713.
- 79 F. M. F. de Groot, M. Abbate, J. van Elp, G. A. Sawatzky, Y. J. Ma, C. T. Chen and F. Sette, Oxygen 1s and cobalt 2p X-ray absorption of cobalt oxides, *J. Phys.: Condens. Matter*, 1993, **5**, 2277–2288.
- 80 V. S. Coker, N. D. Telling, G. van der Laan, R. A. D. Patrick, C. I. Pearce, E. Arenholz, F. Tuna, R. E. P. Winpenny and J. R. Lloyd, Harnessing the Extracellular Bacterial Production

of Nanoscale Cobalt Ferrite with Exploitable Magnetic Properties, *ACS Nano*, 2009, **3**, 1922–1928. Article Online  
DOI: 10.1039/D5EN00379E

81 E. Bartolomé, P. Cayado, E. Solano, S. Ricart, J. Gázquez, B. Mundet, M. Coll, T. Puig, X. Obradors, M. Valvidares, J. Herrero-Martín, P. Gargiani and E. Pellegrin, Magnetic stability against calcining of microwavesynthesized CoFe<sub>2</sub>O<sub>4</sub> nanoparticles, *New J. Chem.*, 2016, **40**, 6890–6898.

82 T. Gaudisson, R. Sayed-Hassan, N. Yaacoub, G. Franceschin, S. Nowak, J.-M. Grenèche, N. Menguy, P. Saintavit and S. Ammar, On the exact crystal structure of exchange-biased Fe<sub>3</sub>O<sub>4</sub>–CoO nanoaggregates produced by seed-mediated growth in polyol, *CrystEngComm*, 2016, **18**, 3799–3807.

83 J. F. Hochepped, P. Saintavit and M. P. Pileni, X-ray absorption spectra and X-ray magnetic circular dichroism studies at Fe and Co L<sub>2,3</sub> edges of mixed cobalt–zinc ferrite nanoparticles: cationic repartition, magnetic structure and hysteresis cycles, *J. Magn. Magn. Mater.*, 2001, **231**, 315–322.

84 W. Baaziz, B. P. Pichon, Y. Liu, J.-M. Grenèche, C. Ulhaq-Bouillet, E. Terrier, N. Bergéard, V. Halté, C. Boeglin, F. Choueikani, M. Toumi, T. Mhiri and S. Begin-Colin, Tuning of Synthesis Conditions by Thermal Decomposition toward Core–Shell Co<sub>x</sub>Fe<sub>1-x</sub>O@Co<sub>y</sub>Fe<sub>3-y</sub>O<sub>4</sub> and CoFe<sub>2</sub>O<sub>4</sub> Nanoparticles with Spherical and Cubic Shapes, *Chem. Mater.*, 2014, **26**, 5063–5073.

85 G. van der Laan and A. I. Figueroa, X-ray magnetic circular dichroism—A versatile tool to study magnetism, *Coord. Chem. Rev.*, 2014, **277–278**, 95–129.

86 V. R. Singh, V. K. Verma, K. Ishigami, G. Shibata, Y. Yamazaki, A. Fujimori, Y. Takeda, T. Okane, Y. Saitoh, H. Yamagami, Y. Nakamura, M. Azuma and Y. Shimakawa, Enhanced ferromagnetic moment in Co-doped BiFeO<sub>3</sub> thin films studied by soft X-ray circular dichroism, *J. Appl. Phys.*, 2013, **114**, 103905.

87 L. Néel, Superparamagnétisme des grains très fins antiferromagnétiques, *Comptes Rendus Hebdomadaires Des Seances De L Academie Des Sciences*, 1961, **252**, 4075–4080.

88 S. Sako, Y. Umemura, K. Ohshima, M. Sakai and S. Bandow, Magnetic Property of Antiferromagnetic MnO Ultrafine-Particle, *J. Phys. Soc. Jpn.*, 1996, **65**, 280–284.

89 L. Zhang, D. Xue and C. Gao, Anomalous magnetic properties of antiferromagnetic CoO nanoparticles, *J. Magn. Magn. Mater.*, 2003, **267**, 111–114.

90 R. Kumar, H. Kumar, M. Kumar and R. R. Singh, Enhanced saturation magnetization in cobalt doped Ni-Zn Ferrite Nanoparticles, *J. Supercond. Nov. Magn.*, 2015, **28**, 3357–3564.

91 S. Thakur, S. C. Katyal and M. Singh, Structural and magnetic properties of nano nickel–zinc ferrite synthesized by reverse micelle technique, *J. Magn. Magn. Mater.*, 2009, **321**, 1–7.

92 A. López-Ortega, M. Estrader, G. Salazar-Alvarez, S. Estradé, I. V. Golosovsky, R. K. Dumas, D. J. Keavney, M. Vasilakaki, K. N. Trohidou, J. Sort, F. Peiró, S. Suriñach, M. D. Baró and J. Nogués, Strongly exchange coupled inverse ferrimagnetic soft/hard, M<sub>n</sub>xFe<sub>3-x</sub>O<sub>4</sub>/ FexMn<sub>3-x</sub>O<sub>4</sub>, core/shell heterostructured nanoparticles, *Nanoscale*, 2012, **4**, 5138–5147.

93 M. Estrader, A. López-Ortega, S. Estradé, I. V. Golosovsky, G. Salazar-Alvarez, M. Vasilakaki, K. N. Trohidou, M. Varela, D. C. Stanley, M. Sinko, M. J. Pechan, D. J. Keavney, F. Peiró, S. Suriñach, M. D. Baró and J. Nogués, Robust antiferromagnetic coupling in hard-soft bi-magnetic core/shell nanoparticles, *Nat. Commun.*, 2013, **4**, 2960.